Numerical Methods in Civil Engineering, 10-1 (2025) 23-30

Numerical Methods in Civil Engineering

Journal Homepage: https://nmce.kntu.ac.ir/

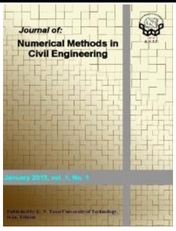

Large Deformation Modeling of Trapdoor Test Using MLS-MPM

Omid Reza Barani *, Amir M. Maleki **

ARTICLE INFO

RESEARCH PAPER

Article history:
Received:
June 2025
Revised:
August 2025
Accepted:
August 2025

Keywords:
Arching,
Trapdoor test,
Moving Least Squares Material Point Method,
Granular media

Abstract:

Moving least squares material point method (MLS-MPM) is a novel approach that enables sharp separation of particles and reduces cell-crossing errors in material point method simulations. This paper uses the MLS-MPM method to numerically simulate the trapdoor test and soil arching, a phenomenon that plays a vital role in the design of many geotechnical structures, such as pile-supported embankments, buried pipelines, tunnels, and trench excavations. Large deformation of soil is considered during the plastic phase of deformation. Non-associated Mohr-Coulomb plasticity is enhanced to capture strain hardening/softening typically seen in granular soils. The proposed method is validated against centrifuge trapdoor tests. The numerical stress fields agree with the formation of a triangular-shaped arch after medium relative displacements and mobilization of a prism of soil after large relative displacements of the trapdoor. It is shown that using MLS-MPM, the arching behavior of soil can be described in detail throughout the trapdoor test.

1. Introduction

Arching is one of the most fundamental phenomena influencing the redistribution of stresses in granular soils at both laboratory and field scales [1]. It affects the earth pressure acting on underground structures and plays a vital role in the design of many geotechnical structures, such as pile-supported embankments, buried pipelines, tunnels, trench excavations to name a few [2]. The arching effect has been extensively studied experimentally through trapdoor tests [1-5].

Several numerical models have been developed to investigate the effect of arching, following two main approaches. The first approach is based on a discrete system, in which individual grains are modeled as rigid bodies, where grain-to-grain force-displacement laws determine the overall behaviour of the system. The class of discrete systems includes the discrete element method [6], the lattice-solid method [7], and the contact dynamics method [8]. High computational costs required to track all grain interactions, the small time-steps required for the solution stability, and the effort needed to constrain bulk properties of the assemblage are some challenges that the discrete approach poses [9-11]. The second approach relies upon a continuum system, where the granular material is modeled as a continuous mass. In this approach, the geometry could be discretized into smaller subdomains. The finite element method (FEM) is an example of this approach. The major drawback of this method is its limited capability in modeling large deformations. Recent developments aim to minimize disabilities of FEM [12]. Combining both previous strategies makes it possible to keep the grains data while using a background mesh to reduce the total number of degrees of freedom and computational costs. An example of such an approach is the material point method (MPM). This method has been successfully used to model landslides [13-15], anchors and geo-interfaces [16-18], and dam failure [19-20]. Moving Least Squares (MLS) is a high-order, accurate method that calculates a polynomial best fit to transfer data between grid nodes and material points. Recently, MLS-MPM was introduced to allow for the sharp separation of material points, an issue that traditional MPM fails to model

**Corresponding author: Associate Professor, Faculty of Civil Engineering, K. N. Toosi University of Technology, Tehran, Iran. Email: barani@kntu.ac.ir*

*** M.Sc. student, Faculty of Civil Engineering, K. N. Toosi University of Technology, Tehran, Iran.*

https://doi.org/10.61882/NMCE.2506.1093

[21]. This method was incorporated to reduce the cell-crossing error in MPM simulations [22], and to successfully model frictional contacts [23], rock avalanches [24], and landslide depositions [25].

In this paper, MLS-MPM, a new numerical tool for the sharp separation of material, is employed to model granular soil arching. In order to consider large deformations that often occur within the failure zone of the soil, a finite strain formulation is utilized during the plastic phase of deformation. Non-associated Mohr-Coulomb plasticity is enhanced to capture strain hardening/softening typically seen in granular soils. The capabilities of MLS-MPM are examined in the simulation of centrifuge trapdoor tests. To the authors' knowledge, it is the first time that the MLS-MPM method is employed to model the trapdoor problem.

2. Formulation

The MLS approximation of the velocity function $v(\boldsymbol{x})$ near a fixed point $\boldsymbol{s}$ is defined as

$$\mathrm{v(x) = P^T(x-s)c(s)} \tag{1}$$

where $\mathrm{P(x-s) = [p_1(x-s), p_2(x-s), \dots, p_{nb}(x-s)]^T}$ forms a complete basis function vector, and $\boldsymbol{c}(\boldsymbol{s})$ is the vector of non-constant basis coefficients that depend on the location where they are computed. In order to determine the unknown basis coefficients, the following weighted Least Squares error is minimized:

$$\mathrm{J(c) = \sum_{I=1}^{n} \omega_I\,(x_I - s)(P^T(x_I - s)c(s) - v(x_I))^2} \tag{2}$$

where $\omega_I(\boldsymbol{s}-\boldsymbol{x}_I)$ is a weighting function centered at $\boldsymbol{x}_I$ .Its role is to define the radius of influence and the weight of neighboring points on the approximation. n is the point number in the surroundings of $\boldsymbol{s}$ for which the weight function is not zero. The coefficient vector is obtained after $\frac{\partial J}{\partial c_I}$ is set to zero for I = 1, 2, . . . , n, leading to the following linear relation:

$$\mathrm{\sum_{I=1}^{n} \omega_I\,(x_I - s)P(x_I - s)(P^T(x_I - s)c(s) - v(x_I)) = 0} \tag{3}$$

Defining

$$\mathrm{D = \sum_{I=1}^{n} \omega_I(x_I - s)\,P(x_I - s)P^T(x_I - s)} \tag{4}$$

and $B = \sum_{I=1}^{n} \omega_I(x_I - s)\,P(x_I - s)v(x_I)$, the coefficients are obtained as:

$$\mathrm{c = D^{-1}B} \tag{5}$$

The MLS solution is given by

$$\mathrm{v(x) = \sum_{I=1}^{n} \omega_I(x_I - s)\,P^T(x-s)D^{-1}P(x_I - s)v(x_I)} \tag{6}$$

In particular, point $\boldsymbol{s}$ may coincide with a material point $\mathrm{x_P}$:

$$\mathrm{v(x) = \sum_{I=1}^{n} \omega_I(x_I - x_P)\,P^T(x-x_P)D^{-1}P(x_I - x_P)v(x_I)} \tag{7}$$

This relation can be written as

$$\mathrm{v(x) = \sum_{I=1}^{n} \Phi_I(x)\,v_I} \tag{8}$$

where $\mathrm{v_I = v(x_I)}$ and

$$\mathrm{\Phi_I(x) = \omega_I(x_I - x_P)P^T(x-x_P)D^{-1}P(x_I - x_P)} \tag{9}$$

is defined as the shape function at $\mathrm{x_I}$ similar to the Element Free Galerkin (EFG) method [26] with the exception that both the basis function and the coefficient vectors in Eq. (1) are functions of x only. However, to prevent numerical difficulties due to large entries in the D matrix, it is preferable to re-center the basis functions [27-28]. Unlike the traditional MPM, which utilizes B-splines for interpolation, the MLS-MPM employs $\mathrm{\Phi_I(x)}$ from Eq. (8) as shape functions. This is the main contribution of MLS-MPM, providing key advantages over traditional MPM. Considering that for B-spline shape functions $\mathrm{N_I(x)}$, $\mathrm{\sum_I N_I(x_I - x_P) = 1}$ (partition of unity) and $\mathrm{\sum_I x_I N_I(x_I - x) = x}$ for any x, it leads to $\mathrm{\sum_I (x_I - x_P)N_I(x_I - x_P) = 0}$ [29]. Thus, we set $\mathrm{\omega_I = N_I}$ and $\mathrm{s = x_P}$ in Eq. (4) and choosing a 2D linear space for the basis function vector $\mathrm{P(x-s) = [1, x-s_x, y-s_y]^T}$ to obtain:

$$\mathrm{D = \sum_{I=1}^{n} \omega_I(x_I - x_P)\begin{bmatrix} 1 & (x_I - x_P)^T \\ (x_I - x_P) & (x_I - x_P)(x_I - x_P)^T \end{bmatrix}}$$

$$= \begin{cases} \mathrm{h^2 I/3} & \text{cubic} \\ \mathrm{h^2 I/4} & \text{quadratic} \end{cases} \tag{10}$$

where I is the unit matrix and h is the grid spacing [29-30]. In this case, $\mathrm{D^{-1}}$ in Eq. (9) is simplified to a constant scaling factor.

The weak form of the momentum conservation equation can be written as:

$$\int_\Omega w_i \rho \dot{v}_i \, d\Omega + \int_\Omega w_{i,k}\sigma_{ik} d\Omega = \int_{\Gamma^t} w_i \bar{t}_i d\Gamma + \int_\Omega w_i \rho b_i \, d\Omega \tag{11}$$

where w_i is the i[th] component of an arbitrary vector-valued test function that is zero at the Dirichlet boundary, ρ is the Eulerian material density, σ is the Cauchy stress tensor, b represents the body force, $\bar{\mathrm{t}}$ is the traction, Ω is the domain, Γ^t is the prescribed traction boundary and $\dot{\mathrm{v}}$ is the rate of the velocity vector. The Eq. (11) should be solved at grid nodes. Dividing the domain with material point partitions Ω_P leads to

$$\sum_P \int_{\Omega_P} w_i \rho \dot{v}_i \, d\Omega + \sum_P \int_{\Omega_P} w_{i,k}\sigma_{ik} d\Omega = \int_{\Gamma^t} w_i \bar{t}_i d\Gamma + \sum_P \int_{\Omega_P} w_i \rho b_i \, d\Omega \tag{12}$$

Using Eq. (8) for the weight function w_i, we have

$$\mathrm{w_i(x) = \sum_{I=1}^{n} \Phi_I(x)\,w_{Ii}} \tag{13}$$

Substituting Eqs. (8) and (13) in Eq. (12), the conservation of momentum can be written as

$$\mathrm{\dot{p} = f^{int} + f^{ext}} \quad , \quad \mathrm{\forall x_I \notin \Gamma_u} \tag{14}$$

where the momentum $\dot{p}$ is defined as

$$\dot{p} = \sum_P \sum_I \sum_J w_{Ii} \dot{v}_{Ji} M_{IJ} \quad (15)$$

$$M_{IJ} = \int_{\Omega_P} \rho \Phi_I(x) \Phi_J(x) d\Omega \approx m_P \Phi_I(x_P) \Phi_J(x_P) \quad (16)$$

where M_{IJ} is the mass matrix and m_P is the material point mass. The internal force vector is expressed as:

$$f^{int} = -\sum_P \sum_I \sum_J w_{Ii} \int_{\Omega_P} \Phi_{I,j} \sigma_{ji} d\Omega \approx -\sum_P \sum_I \sum_J w_{Ii} V_P N_I(x_I - x_P) D^{-1}(x_{Ij} - x_{Pj}) \sigma_{ji} \quad (17)$$

with V_P denoting the current volume of the material point. When displacements are large, the motion is described by the deformation gradient tensor F. In order to consider plastic strains, the deformation gradient tensor is multiplicatively decomposed into elastic and plastic parts as $F = F^e F^p$ with the superscripts e and p representing the pure elastic and pure plastic parts, respectively. In this way, as stress is only related to elastic deformations, the final deformed shape is recognized as a purely elastic mapping from an intermediate, stress-free shape consisting of only plastic deformation [31-32]. The elastic part of the deformation gradient tensor F^e is the conjugate strain measure for the first Piola-Kirshhoff stress in the strain energy ψ. Considering $J = \det(F)$ and substituting $\sigma_{ji} = \frac{1}{J} \frac{\partial \psi}{\partial F^e_{jk}} F^e_{ik}$ and $V_P = J V^0_P$ in Eq. (17):

$$f^{int} \approx -\sum_P \sum_I \sum_J w_{Ii} V^0_P N_I(x_I - x_P) D^{-1} \left(x_{Ij} - x_{Pj}\right) \frac{\partial \psi}{\partial F^e_{jk}} F^e_{ik} \quad (18)$$

where V^0_P denotes the reference volume of the material point. The external force vector is described as:

$$f^{ext} = f^{ext}_b + f^{ext}_t \quad (19)$$

where

$$f^{ext}_b = \sum_P \sum_I \sum_J w_{Ii} \int_{\Omega_P} \Phi_I(x) b_i d\Omega \approx \sum_P \sum_I \sum_J w_{Ii} \Phi_I(x_P) b_i J V^0_P \quad (20)$$

is the external body force and f^{ext}_t is the external traction force.

Large-displacement, small-strain problems can be addressed using corotational formulation in which a linear stress-strain relation is assumed for simplicity, while invariance under large rigid body motions is assured. In this formulation, since F is invertible, the polar decomposition theorem yields to decomposition of the deformation and expresses F as the product of an orthogonal rotation tensor R and a symmetric Cauchy stretch tensor U or V [33]:

$$F = VR = RU \quad (21)$$

The rotation R transfers the principal axes of strain at the reference shape into the principal axes of strain at the present shape.

It is noted that the symmetric tensor U can be decomposed as

$$U = QSQ^T \quad (22)$$

where Q is a rotation matrix whose columns are the normalized eigenvectors of U and S. Substituting Eq. (22) in Eq. (21) gives:

$$F = RU = RQSQ^T = WSQ^T \quad (23)$$

which is the common form of singular value decomposition (SVD) of the matrices. Accordingly, the singular value decomposition of the elastic part of the deformation gradient tensor yields $F^e = W^e S^e Q^{eT}$. Eliminating rotation from the elastic part of the deformation gradient tensor, a linear strain tensor is defined as $\varepsilon^e = S^e - I$ where I is the identity tensor. The strain energy function in the corrected corotational model is defined as [34]:

$$\psi(F^e) = \mu \sum_i \varepsilon_i^{e2} + \frac{\lambda}{2}(J-1)^2 \quad (24)$$

where μ and λ are Lame constants.

The soil behavior can be described using non-associated Mohr-Coulomb plasticity [35-36]. Following [37], the non-associated Mohr-Coulomb plasticity is enhanced to capture strain hardening/softening typically seen in brittle materials. Defining $p = \frac{\sigma_1 + \sigma_3}{2}$ and $q = \frac{\sigma_1 - \sigma_3}{2}$ where σ_1 and σ_3 are the maximum and minimum principal stresses, respectively, the Mohr-Coulomb yield criterion is expressed as

$$q = c \cos \varphi + p \sin \varphi \quad (25)$$

where c and φ are cohesion and internal friction angle, respectively. Similar to [35], the strength parameters (cohesion and internal friction angle) are evaluated using the following rules:

$$c = c_r + (c_{peak} - c_r) e^{-\eta \varepsilon^p_{eq}} \quad (26)$$

$$\varphi = \varphi_r + (\varphi_{peak} - \varphi_r) e^{-\eta \varepsilon^p_{eq}} \quad (27)$$

where subscript r denotes residual value, η is a shape factor parameter controlling the rate of strength increase/decrease, and ε^p_{eq} is equivalent plastic strain is defined as

$$\varepsilon^p_{eq} = \sqrt{\frac{2}{3} e^p : e^p} \quad (28)$$

where $\boldsymbol{e}^p$ denotes the deviatoric part of the plastic strain tensor. It is well known that the softening part of stress-strain curves in quasi-brittle materials is not a material property. Therefore, special care should be given where different mesh sizes are used in a standard continuum model consisting of a strain-softening material. In this case, the crack band model [38] could be used as a regularization technique to avoid mesh dependency in a strain-localization problem. According to the crack band model, the total dissipated strain energy by a shear band should be the same for different element sizes. In the material point method, the thickness of a shear band is approximated by the grid element size [38]. It was shown that if the shape factor parameter η varies in a direct manner with the element size, the problem solution becomes independent of the grid size. In this study, only one grid size was utilized for each model. Thus, only one shape factor parameter is needed for each problem.

In the MLS-MPM method, similar to MPM, a continuum body is divided into discrete material points that travel across a background mesh. The material point physical properties, including velocity and stress, are mapped onto the mesh. The momentum equation is solved on this mesh, which then deforms according to the updated nodal velocities. Finally, the material point states are adjusted based on the mesh deformation. In the MLS-MPM method, smooth shape functions from Eq. (9) are utilized to reduce the error corresponding to the material point cell-crossing.

3. Trapdoor test modeling

Centrifuge tests have been widely used for physical modeling of geotechnical problems. The main idea for geotechnical centrifuge testing is to replicate field conditions on a smaller scale accurately. Since soil behavior is strongly inspired by stress levels, it is crucial to make sure that stresses in the model correspond to those in the actual prototype for proper similitude. Geotechnical centrifuge experiments utilize rotational motion to generate centripetal acceleration, which simulates gravitational effects. By increasing gravitational acceleration in the centrifuge, small-scale models can effectively model real-world conditions while using the same materials as the full-scale prototype [39-40].

The trapdoor test is useful for understanding soil arching around geotechnical structures such as tunnels and anchor plates. In this section, centrifuge trapdoor tests [39-40] are modelled numerically to show MLS-MPM capabilities in the simulation of active soil arching problems. The experimental model consists of a strip trapdoor that can move downward while the geomaterial experiences centripetal acceleration. The tests were conducted using a Genisco beam-type geotechnical centrifuge, which has an effective radius of approximately 1.7 meters. With increasing downward displacement of the trapdoor (at a speed of 0.18 mm/s), the load change on it was monitored during the test using a high-speed data acquisition system. The soil-containing box had interior dimensions of 406 mm, 330 mm, and 254 mm in length, width, and height, respectively. The edges of the trapdoor segments were tapered slightly to minimize friction with the side walls. Thus, wall friction was not considered in the numerical model.

Uniform coarse sand ($C_u = \frac{D_{60}}{D_{10}} = 1.7mm$) with subangular grains passed through the #4 (4.76 mm) sieve and retained on the #14 (1.41 mm) sieve was used in their experiments. The average particle size was 2.1 mm, and the specific gravity was measured as 2.66. The peak friction angle of 39° had been measured from direct shear tests for a void ratio of 0.70 and normal stress levels of 49 kPa and 98 kPa. The soil was poured into trowel-sized scoops and scattered manually. The pouring of the grains represented regular packing. The average bulk density prior to mounting on the centrifuge platform was around 1600 kg/m^3. The gravitational acceleration was increased in a centrifuge apparatus until the desired highest acceleration was reached. Gravity accelerations of 80g were applied to the soil. Afterward, the trapdoor was moved downward, causing a decrease in the load on the trapdoor. The load was reported on the central part of the trapdoor.

Figure 1 shows a typical plot of average normalized vertical stress on the trapdoor versus the normalized trapdoor vertical displacement based on data from centrifuge experiments by [40]. In this figure, the average vertical stress on the trapdoor (p) is normalized with the theoretical geostatic stress ($p_0 = \gamma H$) while trapdoor vertical displacement (δ) is normalized with respect to the trapdoor width (B). As shown in this figure, upon trapdoor lowering, the vertical stress on the trapdoor falls sharply below the theoretical overburden pressure down to a point where the curvature is greatest and is called the breakpoint, while the load starts to redistribute, which increases the adjacent soil stresses. As a result of active soil arching and the development of initial slip surfaces above the trapdoor, the load on the trapdoor stabilizes to a minimum value, and the stress decrease diminishes. As the trapdoor lowering continues, the vertical stress on the trapdoor slowly increases until the trapdoor reaches its maximum achievable displacement. This slight increase shows that only a limited volume of soil above the trapdoor follows the trapdoor lowering. The reason for this increase may be a change in the configuration of slip surfaces from a curved shape to a triangular one [38]. The numerical model consists of a trapdoor, a soil layer, and a void zone below the trapdoor.

As shown in Figure 2, both lateral sides are fixed in the horizontal direction while the bottom is fixed in the vertical direction in the quasistatic part of the simulation. In the dynamic stage, the trapdoor moves down with a vertical velocity set to 0.18 mm/s. Gravity acceleration is applied to the model in the quasistatic part of the simulation and remains constant during the dynamic stage.

A structured grid with 0.005-m element size was utilized to discretize the model in space, ensuring converges to a unique solution. An adaptive time-stepping scheme with a minimum time step of 10^{-5} s was used for discretization in time to prevent numerical instability. The geometrical parameters are chosen according to [37-38] and are presented in Table 1. Mohr-Coulomb plasticity model with strain softening, as described in section 4, is assumed for the soil. Material properties for soil are presented in Table 2. Similar material properties are considered for the numerical modeling of this problem using MPM [41].

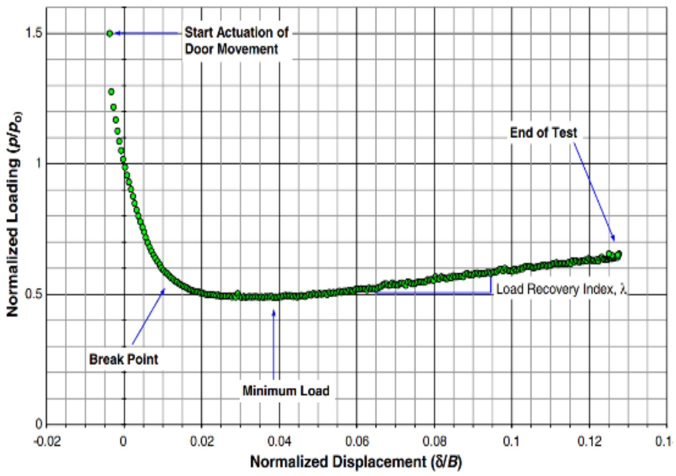

Fig. 1: A typical plot of average normalized vertical stress versus normalized trapdoor vertical displacement [39]

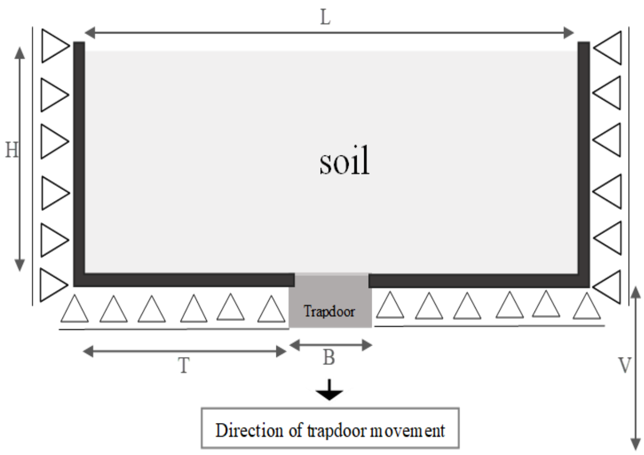

Fig. 2: Scheme of the model and boundary conditions

Table 1: Geometrical parameters

Description	Symbol	Unit	Value
Trapdoor length	B	m	0.05
Soil layer height	H	m	0.05, 0.1, 0.125, 0.2
Soil layer length	L	m	0.4
Void zone height	V	m	0.05
Distance to trapdoor edge	T	m	0.1875
Soil layer thickness	W	m	0.01

Table 2: Soil material parameters

Material property	Symbol	Unit	Value
Density	ρ	$\frac{kg}{m^3}$	1600
Elasticity modulus	E	MPa	8
Poisson's ratio	ν	-	0.3
Peak friction angle	φ_{peak}	$^\circ$	35
Residual friction angle	$\varphi_{Residual}$	$^\circ$	30
Peak cohesion	C_{peak}	MPa	0
Residual cohesion	$C_{Residual}$	MPa	0
Shape factor	η	-	500

Figure 3 presents vertical and horizontal stress contours at the end of the quasistatic stage. Tensile stress is assumed to be positive. Stresses at the end of the quasistatic stage are considered as initial stresses for the dynamic stage. Figures 4-6 illustrate the impact of overburden from experiments GI197–GI200 [40] highlighting the break point, end of the test point, and minimum load point, representing three main state points of tests. Figure 4 presents the average stress versus depth of soil normalized with the trapdoor width. As shown in Figure 4, the minimum absolute stress values for different soil depths are the same. The roughly constant minimum vertical stress and stress at the end of the test for all models is attributed to the same volume and weight of soil below the stable arch for all overburden depths equal to or greater than the width of the trapdoor.

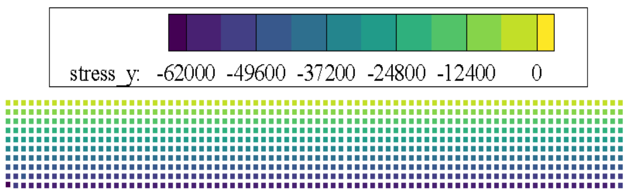

(a)

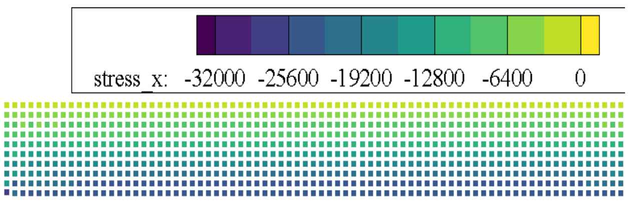

(b)

Fig. 3: The soil layer initial stresses (a) vertical stress (Pa), (b) horizontal stress (Pa)

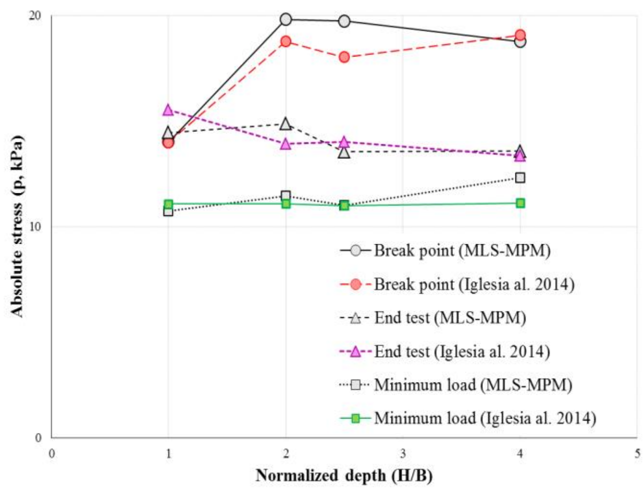

Fig. 4: Numerical average stress on trap door versus normalized depth compared to experimental results

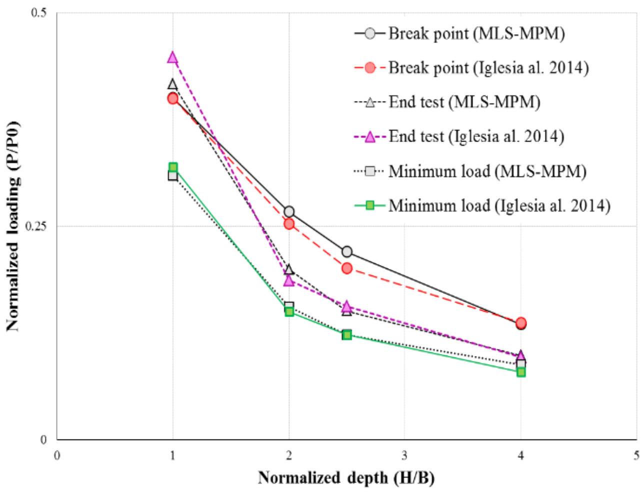

Fig. 5: Numerical normalized loading on trap door versus normalized depth compared to experimental results

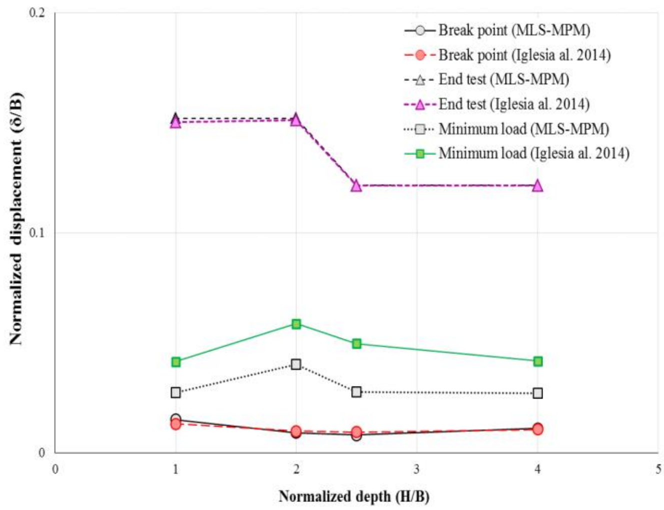

Fig. 6: Numerical normalized displacement of the trapdoor versus normalized depth compared to experimental results

Figure 5 illustrates normalized loading stress vs. normalized depth of soil. Since the change in absolute stress values with normalized depth variation is small, the normalized loading stress for all cases reduces when the soil depth is increased. As seen in Figure 5, the trends of the break point and minimum point stresses are similar. The stress at the end of each test is generally between the minimum and break point stresses, except for the case of H/B=1, in which the arching action may not be fully sustained due to the soil shallow depth [40]. Figure 6 shows normalized displacement versus normalized soil depth. As shown in this figure, the normalized displacement at the break point is the same in all cases, irrespective of the depth of overburden, while the value of normalized trapdoor displacement is roughly the same in all cases at the minimum loading point and at the end of the test. The numerical results are in full agreement with experimental data at the break point and end of each test.

Figure 7 and Figure 8 represent horizontal and vertical stress evolution during the trapdoor test, respectively, for a 7 cm soil layer height. Tensile stress is assumed to be positive. As shown in Figure 7, with the downward movement of the trapdoor, the compressive horizontal stress in the soil above the trapdoor increased significantly due to the soil arching. However, a small portion of the soil next to the trapdoor does not participate in the load transfer. In this thin layer of soil, the compressive horizontal stress is reduced. As Figure 8 illustrates, the vertical stress above the trapdoor reduces significantly during the downward movement of the trapdoor, while the vertical stress at both sides of the trapdoor increases due to arching of soil particles. As Figures 7-8 show, the detailed process of stress transfer due to arching during the trapdoor test can be evaluated using the MLS-MPM method. The numerical stress fields agree with the formation of triangular-shaped arch after medium relative displacements and mobilization of a prism of soil after large relative displacements of the trapdoor.

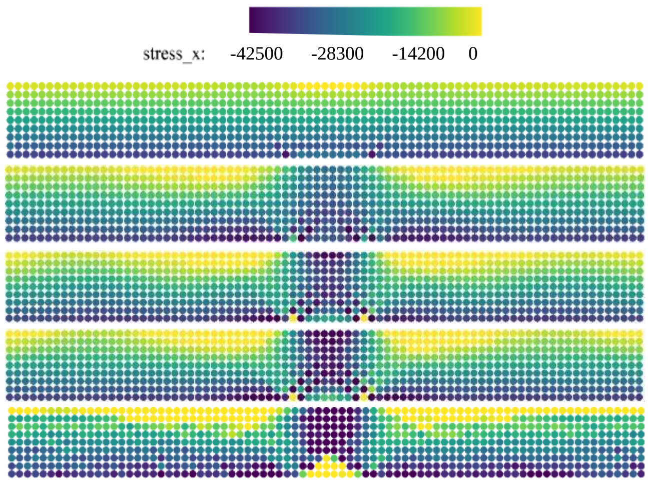

Fig. 7: Horizontal stress (Pa) during trapdoor test

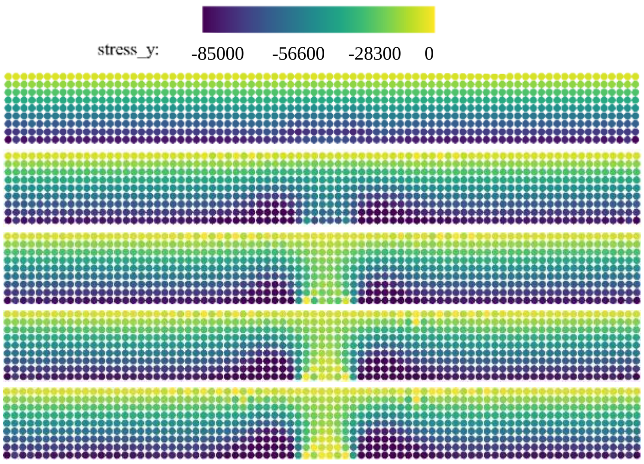

Fig. 8: Vertical stress (Pa) during trapdoor test

4. Conclusions

This paper uses the MLS-MPM method to numerically simulate the arching of soil grains during the trapdoor test. Large deformation of soil was considered during the plastic phase of deformation. Non-associated Mohr-Coulomb plasticity was enhanced to capture strain hardening/softening typically seen in granular soils. The proposed method was validated against centrifuge trapdoor tests. Results of the numerical model exhibited strong agreement with experimental data. The numerical stress fields agreed with the formation of triangular shaped arch after medium relative displacements and mobilization of a prism of soil after large relative displacements of the trapdoor. It was shown that using MLS-MPM, the mechanical behaviour of the soil can be described throughout the trapdoor test.

References

[1] Terzaghi, K., 1936. Stress distribution in dry and saturated sand above a yielding trapdoor. Proceedings 1st Conference on Soil Mechanics and Foundations Engineering, Graduate School of Engineering. Harvard University, Cambridge, MA, 307-311.

[2] Costa, Y. D., Zornberg, J.G., Bueno, B.S., and Costa, C. L., 2009. Failure mechanisms in sand over a Deep active trapdoor. Journal Geotechnical and Geoenvironmental Engineering. 10.1061/(ASCE)GT.1943-5606.0000134, 1741-1753.

[3] Engesser, Fr., 1882. Ueber den Erdduck gegen innere Stüzwande (Tunnelwande). Deutsche Bauzeitung, 16, 91-93 (in German).

[4] Iglesia G. R., 1991. Trapdoor experiments on the centrifuge: a study of arching in geomaterials and similitude in geotechnical models. Ph.D. thesis, Massachusetts Institute of Technology, Cambridge.

[5] Dewoolkar, M. M., Santichaianant, K., and Ko, H.-Y., 2007. Centrifuge modelling of granular soil response over active circular trapdoors. Soils and Foundations 47(5),931-945.

[6] Cundall, P. A., Strack, O. D. L., 1979. A discrete numerical model for granular assemblies. Geotechnique 29, 47-65.

[7] Mora, P., Place, D., 1993. A lattice solid model for the non-linear dynamics of earthquakes. International Journal of Modern Physics. C 4, 1059-1074.

[8] Radjaï, F., Dubois, F., 2011. Discrete-element Modeling of Granular Materials. Wiley-Iste, Hoboken, New Jersey, USA.

[9] Tu, X. and Andrade, J. E., 2008. Criteria for static equilibrium in particulate mechanics computations, International Journal for Numerical Methods in Engineering 75, 1581–1606.

[10] Gray G. G., Morgan J. K., and Sanz P. F., 2014. Overview of continuum and particle dynamics methods for mechanical modeling of contractional geologic structures. Journal of Structural Geology. 59, 19–36.

[11] Lim, K.-W. Krabbenhoft, K., and Andrade, J.E., 2014. A contact dynamics approach to the Granular element method, Computer Methods in Applied Mechanics and Engineering 268, 557–573.

[12] Seyyedan, S. M., Mirghasemi, A. A., Mohammadi, S., 2021. Numerical simulation of direct shear test on granular materials composed of breakable angular particles: A DEM-XFEM approach. Powder Technology 391, 450-466.

[13] Andersen, S. and Andersen, L., 2010. Modelling of landslides with the material-point method. Computational Geosciences 14 (1), 137-147.

[14] Barani, O., and Bagherzadeh, H., 2023. Simulation of the Vaiont landslide via multi-body material point method with cohesive frictional interfaces. Scientia Iranica 30, 902-917.

[15] Zhang, W., Wu, Z., Peng, C., Li, S., Dong, Y., and Yuan, W., 2023. Modelling large-scale landslide using a GPU-accelerated 3D MPM with an efficient terrain contact algorithm. Computer and Geotechnics 158, 105411

[16] Coetzee, C., J., Vermeer, P., A., and Basson, A., H., 2005. The modelling of anchors using the material point method. International Journal for Numerical and Analytical Methods in Geomechanics 29 (9), 879-895.

[17] Fetrati, M., Galavi, V., Goodarzi, M., Mörz, T., and Kreiter, S., 2024. Simulation of cone penetrometer tests in sand using three advanced constitutive models: a comparative study. Computers and Geotechnics 176, 106683.

[18] Galavi, V., Martinelli, M., 2024. MPM simulation of the installation of an impact driven pile in dry sand and subsequent axial bearing capacity. Journal of Geotechnical and Geoenvironmental Engineering 150 (4), 04024019.

[19] Alonso, E. and Zabala, F., 2011. Progressive failure of Aznalc_ollar dam using the material point method. Geotechnique 61 (9), 795-808.

[20] Talbot, L., E., D, Given, J., Tjung, E., Y., S., Liang, Y., Chowdhury, K., Seed, R., and Soga, K., 2024. Modeling large-deformation features of the Lower San Fernando Dam failure with the material point method. Computers and Geotechnics 165(2), 105881.

[21] Hu, Y., Fang, Y., Ge, Z., Qu, Z., Zhu, Y., Pradhana, A., Jiang, C., 2018. A moving least squares material point method with displacement discontinuity and two-way rigid body coupling. ACM Transactions on Graphics. 37 (4), 1–14.

[22] Song, J., U., and Kim, H., G., 2021. An improved material point method using moving least square shape functions. Computational Particle Mechanics. 8(4), 751–766.

[23] Nakamura, K., Matsumura, S. and Mizutani, T., 2021 Particle-to-surface frictional contact algorithm for material point method using weighted least squares Computers and Geotechnics 134, 104069.

[24] Zhao, S., He, S., Li, X., Scaringi, G., Liu, Y., Deng, Y., 2024. Investigating the dynamic process of a rock avalanche through an MLS-MPM simulation incorporated with a nonlocal μ(I) rheology model. Landslides. 21, 1483–1499.

[25] Zhao, S., Liu, Y., Scaringi, G., Li, X., He, S., He, G., Zhu, L., 2025. Non-local μ(I) rheology improves landslide deposition modeling in MLS-MPM simulations. Engineering Geology. 348, 107963.

[26] Belytschko, T., Lu, Y., and Gu, L., 1994. Element-free Galerkin methods. International Journal for Numerical Methods in Engineering 37(2), 229–256.

[27] Liu, W., K., Li S. and Belytschko, T., 1997. Moving least square reproducing kernel methods Part I: Methodology and convergence. Computer Methods in Applied Mechanics and Engineering. 143(1-2), 113-154.

[28] Huerta, A., and Fernandez-Mendez, S., 2000. Enrichment and coupling of the finite element and meshless methods. International Journal for Numerical Methods in Engineering. 48(11), 1615-1636.

[29] Jiang, C., Schroeder, C., Selle, A., Teran, J., and Stomakhin, A., 2015. The affine particle-in-cell method, ACM Transactions on Graphics. 34(4), 1-10.

[30] Jiang, C., Schroeder, C., and Teran, J., 2017. An angular momentum conserving affine-particle-in-cell method, Journal of Computational Physics. 338, 137-164.

[31] Simo, J., C., 1988. A framework for finite strain elastoplasticity based on maximum plastic dissipation and the multiplicative decomposition: Part I. continuum formulation. Computer Methods in Applied Mechanics and Engineering, 66(2), 199–219.

[32] Mast, C., 2013. Modeling landslide-induced flow interactions with structures using the Material Point Method. PhD thesis. University of Washington, USA.

[33] Truesdell, C., A., 1991. A First Course in Rational Continuum Mechanics, Academic Press, San Diego, USA.

[34] Stomakhin, A., Howes, R., Schroeder, C., and Teran, J., 2012. Energetically consistent invertible elasticity. In Proceeding of ACM SIGGRAPH/Eurographics Symposium on Computer Animation, 25–32.

[35] Soga, K., Alonso, E., Yerro, A., Kumar, K. and Bandara, S., 2016. Trends in large deformation analysis of landslide mass movements with particular emphasis on the material point method. Géotechnique 66(3), 248–273.

[36] Payan, M., Fathipour, H., Hosseini, M., Chenari, R. J., and Shiau, J. S. 2022. Lower bound finite element limit analysis of geo-structures with non-associated flow rule. Computers and Geotechnics, 147, 104803.

[37] Hosseini, M., B. Yaghoobi, P. Z. Ranjbar, M. Payan, and R. J. Chenari. 2023.Stability analysis of geosynthetic-reinforced shallow foundations with a lower-bound FELA approach adopting the nonassociated plastic flow rule. International Journal of Geomechanics, 23(2), 04022280.

[38] Bazant, Z.P., Oh, B.-H., 1983. Crack band theory for fracture of concrete. Materials and Structures 16, 155–177.

[39] Iglesia ,G., R., Einstein, H., H., and Whitman, R., V., 2011. Validation of centrifuge model scaling for soil systems via trapdoor tests. Journal of Geotechnical and Geoenvironmental Engineering. 137 (11), 1075-1089.

[40] Iglesia ,G., R., Einstein, H., H., and Whitman, R., V., 2013. Investigation of soil arching with centrifuge tests. Journal of Geotechnical and Geoenvironmental engineering. 140(2), 04013005.

[41] Barandiaran Villegas L., B., 2018. Sinkhole development over karstic substratum. An MPM approach. Master's thesis, Universität Politecnica de Catalunya.